




Analysis of thermal history effects on mechanical anisotropy of 3D-printed polymer matrix composites via in situ X-ray tomography

J. C. E. Mertens¹, K. Henderson¹, N. L. Cordes¹, R. Pacheco¹, X. Xiao², J. J. Williams³, N. Chawla³, and B. M. Patterson^{1,*} 

¹ Materials Science and Technology Division, Los Alamos National Laboratory, P.O. Box 1663, Los Alamos, NM 87545, USA

² Argonne National Laboratory, Advanced Photon Source, Lemont, IL 60439, USA

³ Materials Science and Engineering, Arizona State University, Tempe, AZ 85287, USA

Received: 26 April 2017

Accepted: 29 June 2017

Published online:

6 July 2017

© Springer Science+Business Media, LLC 2017

ABSTRACT

The tensile behavior of an additively manufactured (AM) polymer matrix composite (PMC) is studied with in situ X-ray computed microtomography (CT) and digital volume correlation (DVC). In this experiment, the effects of recycled material content and print direction on the selective laser-sintered (SLS) material's mechanical response are explored. The PMC samples are printed in a tensile specimen geometry with gage lengths parallel to all three orthogonal, primary sintering directions. In situ tensile-CT experiments are conducted at Argonne National Laboratory's Advanced Photon Source 2-BM beamline. Analysis of the AM PMC's tensile response, failure, and strain evolution is analyzed both from a conventional standpoint, using the load–displacement data recorded by the loading fixture, and from a microstructural standpoint by applying DVC analysis to the reconstructed volumes. Significant variations on both strength and ductility are observed from both vantages with respect to print direction and the recycled material content in the printed parts. It is found that the addition of recycled source material with a thermal history reduces the tensile strength of the SLS composite for all directions, but the effect is drastic on the strength in the layering direction.

Introduction

Over the last decade, additive manufacturing (AM), or '3D printing,' has become an increasingly popular means for part fabrication [1, 2]. Additive manufacturing shows potential over traditional

manufacturing techniques in several areas [3]. With minimal machining requirements, 3D printing enables part fabrication with less material waste and labor requirements, leading to a relatively low part cost [4]. Conventional manufacturing solutions involving the costly assembly of many individual

Address correspondence to E-mail: bpatterson@lanl.gov

components can be greatly simplified by directly fabricating the assembled components into a single part with AM techniques [5, 6]. Another advantage of AM is the ability to achieve complex part geometries, for example, tortuous internal cavities such as high-aspect-ratio cooling channels, which are otherwise impossible to manufacture [7, 8]. Similarly, additive manufacturing provides the opportunity to implement computational design optimization to determine part geometries which provide ideal performance [9]. Finally, 3D printing enables rapid prototyping and quick concept validation, decreasing the time between part design and part manufacturing [10]. For these reasons, interest in AM techniques is growing.

Three-dimensional printing, as the name implies, is based on building up material layer by layer, where material is bonded to the surrounding material in each layer, and each consecutive layer is bonded to the previous layer below. 3D printing processes typically either rely on actually depositing the material at each desired coordinate, or rely on bonding or polymerizing loose material which already exists freely in the plane of printing. By consecutively printing each individual cross section of the part, the entire part is achieved. Techniques for AM include, but are not limited to, selective laser sintering (SLS) [11], selective laser melting (SLM) [12], and fused deposition modeling (FDM) [13]. Many AM techniques are applicable to both polymeric and metallic material systems [1]. However, AM-derived material is still inherently plagued by defects and flaws as a result of the AM process rendering it inferior to material processed by more conventional, better studied, time-tested processes such as extrusion [14]. Thus, research toward understanding AM-induced microstructures and the resulting effect on AM material performance is paramount to the AM community and their ultimate suitability in high-performance applications.

Two aspects of SLS-printed polymeric material are investigated in the current study: Print anisotropy and the effect of fabrication using recycled print bed material which has thermal history from previous cycles. In SLS, a vat of loose thermoplastic powder is used from which the printed part is generated. The vat is heated to near the melting temperature of the thermoplastic, and a laser is focused on the loose powder at coordinates where bonding is desired. Typically, most of the material in the vat is not

incorporated into the printed part or parts. In order to reduce cost and material waste in SLS printing, it is common to reuse material from previous print cycles [1]. However, as the recycled material has a thermal history, degradation of the unused material can occur [15], which may potentially alter the printed material's properties. Another effect of interest in SLS AM is anisotropy stemming from the printing method where 2D sections of the part are sintered in place before lowering the sintered part, applying additional particle stock above the part, and sintering the next layer, and repeating this process in a layer-by-layer fashion [11]. This work also aims to investigate the mechanical anisotropy of SLS-printed material with respect to the various print directions. The primary directions of interest are the two orthogonal directions in the printing plane and the third direction orthogonal to the print plane and the individually printed layers. Based on difference in the sintering mechanism in-layer and between-layers, the properties can vary in the various print directions. This variation has been reported for direct energy deposition AM metallic material [16], direct metal laser melting [17], FDM polymeric material [18], and vat photopolymerization material [19].

Over the last two decades, X-ray computed tomography (CT) has emerged as a powerful technique for studying microstructural evolution volumetrically, as a result of the technique's ability to acquire 3D structural information at relevant length scales and nondestructively. It follows that this technique offers a unique setting for studying AM microstructures and understanding damage evolution in response to mechanical stimuli, whether conducted at synchrotron X-ray beamlines or using laboratory-scale instrumentation. CT has been applied to the study of polymeric AM structures [20], to metallic AM structures [21], to tensile properties of AM material [16, 22], to in situ compression properties of AM material [23], and even to fatigue of AM material [24, 25].

In this study, we apply synchrotron X-ray CT imaging at 4 Hz (4 completely unique tomograms per second) with in situ tensile loading to study damage evolution in the microstructure of a SLS glass particle-filled polyamide-12 composite material. In essence, the data acquired in this study are four dimensional, providing time-resolved three-dimensional spatial information of a material's dynamic response to a mechanical stimulus. Three different

compositions in terms of recycled powder bed material content are studied, ranging from 0% recycled to 50% recycled. For each composition, two in-print-plane and the between-print-plane directions are investigated. Due to the highly viscoplastic behavior of thermoplastic materials, synchrotron X-ray CT is preferred for imaging tension in situ, as laboratory-scale CT requires lengthy scans during which relaxation may take place [26, 27]. In this experiment, we also measure strain evolution in the polymer matrix composite (PMC) microstructure. Digital image correlation (DIC) has been previously applied to the study of AM material strain evolution [28]; however, DIC leverages 2D imaging and is limited to surface analysis only. Due to the nature of the dynamic CT imaging here implemented, and the nature of the PMC's microstructural features, the data acquired are ideal for volumetric strain evolution mapping in the PMC microstructure via digital volume correlation (DVC).

The present work demonstrates several novelties in the study of the mechanical behavior of additive manufactured material. One novel aspect of the current work comes directly from the experimental approach, leveraging in situ imaging toward the study of tension-induced damage evolution within the AM microstructure. Similarly, the current study utilizes very high temporal resolution of 4 Hz CT data acquisition rates in the study of volumetric microstructural evolution in a PMC. Through this approach, this study reports the deteriorative effects of SLS powder bed material recycling from a mechanical performance vantage. Additionally, this work explores print anisotropy effects in a SLS composite material through high-temporal-resolution 3D imaging. Based on the unique characteristics of the data obtained in this study, this work implements DVC to gain insight into strain and damage evolution volumetrically and at the microstructural scale in an AM microstructure. By coupling high-speed 4D tomographic imaging with mechanical testing and DVC, a wealth of information on the mechanical effects of recycled SLS powder material in conjunction with print direction anisotropy is gained at a far field and microstructural scale. Thus, the experimental approach and analysis in this study of an additively manufactured thermoplastic composite under tensile loading provide new and unique insight into the relationship between processing, microstructure, and performance.

Materials and methods

Sample preparation

The samples in this study were printed directly into a dogbone geometry for mechanical testing. A series of samples were printed with differing amounts of recycled content and in several print orientations. A Formiga P 110 printer manufactured by EOS (Electro Optical Systems, Krailling, Germany) was used to fabricate the test specimens by SLS. The material that was chosen for the study was a propriety blend, PA (polyamide) 3200 GF (glass filled) (Electro Optical Systems, Krailling, Germany), which consisted of a polyamide-12 powder and spherical borosilicate glass particles. The average grain size of the powder stock material was 57 μm as reported by the manufacturer, and the average density of the SLS-produced parts was 1.22 g cm^{-3} . The density variation between the builds was minimal at 0.1 g cm^{-3} , decreasing with recycling. The dogbone test samples were all printed using the same 3D drawing. The CAD drawings were scaled 2.4% in the X and Y axis and 1.9% in the Z axis to reduce the effects of shrinkage.

To study the mechanical response of the printed parts along different print directions, the orientation of the gage length in the print layout was rotated to align with two orthogonal directions in the sintering plane (referred to as X and Y directions) and additionally in the direction perpendicular to the plane in which each consecutive layer was laser sintered (referred to as the Z direction) in the construction of the part (see Fig. 1b). The laser scan pattern used for sintering was such that throughout most of the build, the X direction was the fast sintering direction, the Y direction was the intermediate-speed sintering direction, and the Z direction was the slowest sintering direction. However, during sintering process for a given XY plane, the perimeter of the parts' cross section was sintered before the interior. During printing, the powder bed and contained source material were heated to 169 $^{\circ}\text{C}$, just below the melting temperature of the material of 172–180 $^{\circ}\text{C}$, and material in the build removal chamber was heated to 150 $^{\circ}\text{C}$. All the tensile specimens were printed in the optimal central region of the print bed to minimize thermal gradients that could result in part curling and deformation. During printing, each tensile specimen was placed at least 5 mm away from each

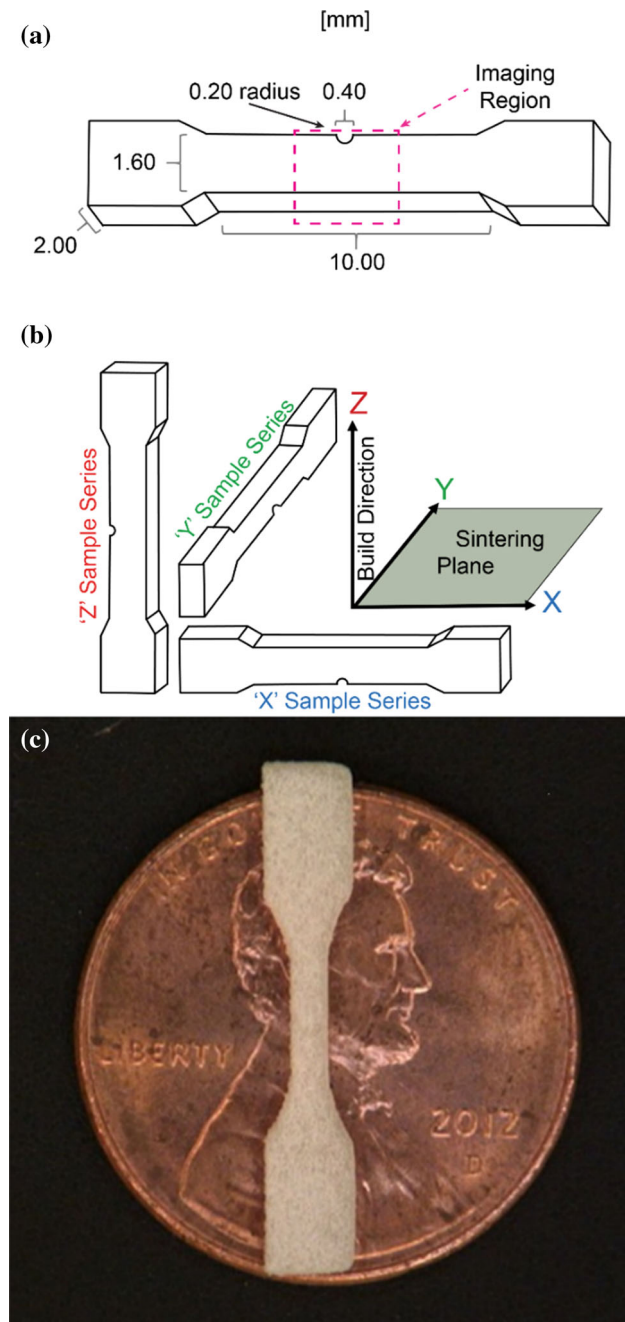


Figure 1 Schematic of **a** the tensile specimen geometry (not to scale), **b** the tensile specimen sample print layout for the study of mechanical anisotropy with print direction, and **c** a photograph of an actual tensile sample shown for scale with a US penny.

neighboring part and at least 6 mm from the bottom powder layer. All the tensile specimens in the present study were made in a single print cycle. The tensile specimens were printed using a 30-W CO₂ laser, and after sintering cooled at a rate of 1.5 °C min⁻¹. After printing, residual surface material was cleaned at a

breakout station by sieving loose powder and blowing off loose particles from the surface using compressed air.

After sintering of the parts was complete, the parts were removed, and the process repeated. The powder bed material that was not sintered into the previous parts was reused. This material is referred to as 'recycled material.' Powder stock that was not in the printer for any previous print cycles is referred to as 'virgin material.' The recycled material had a thermal history from previous print cycles. It was unknown whether the inclusion of recycled material in sample preparation for this experiment would affect the quality of the sintered particle interface with the neighboring particles or the previously sintered layers, or through the microstructure of the stock particles themselves. To investigate recycled material mechanical degradation effects, dogbone specimens with their gage lengths aligned in each print direction were prepared with three blends with varying proportion of virgin material and recycled material. The virgin–recycled proportion of the blends in this study were 100–0, 70–30, and 50–50. The recycled powder was mixed for 5 min with the virgin powder and/or other recycled powder using a cement mixer, stored for 24 h in a metallic container to dissipate electrostatic charge, and returned to the printer's powder bed before sintering the blended tensile specimens.

The samples investigated in this study will be referred to as X50, X70, X100, Y50, Y70, Y100, Z50, Z70, and Z100, where the letter indicates the print direction parallel to the gage length and the number indicates the amount of virgin material used in the powder bed in the printing of the tensile specimens. The tensile specimens were 'flat' dogbones, with a rectangular cross section in the grip and gage length regions. The dogbone geometry has a grip section on either end of the part, and a narrowed region in the center of the part as the gage length. In order to ensure that the failure process was captured by high-resolution X-ray tomography, where the field of view was limited to 3.4 mm in the vertical direction, a small, round notch was placed into the center of the gage length. The notch was made in the sample during printing. The sample print design dimensions are provided in Fig. 1a, and a schematic of the dogbone layout for the orientation study is provided in Fig. 1b. A photograph of one of the printed tensile specimens is provided in Fig. 1c. It is worth noting that for the Z series specimens, all had the Y print

direction parallel to the notch length, the Y-series specimens had the X print direction parallel to the notch length, and the X series samples had the Y print direction parallel to the notch length. It is expected that the material properties along the direction parallel to loading direction will dominate the mechanical behavior. While the effects of notch orientation within the cross section of the X, Y, and Z series samples should not be discounted, it is not included as a factor in this study.

Microtomography

X-ray microtomography was performed at Argonne National Laboratory's Advanced Photon Source, Beamline 2-BM, Hutch A. A schematic of the X-ray imaging and mechanical testing configuration is provided in Fig. 2. The beamline was configured for pink beam imaging, in order to achieve higher X-ray intensity for high-speed imaging. The energy of the polychromatic 'pink' beam ranged from 15 to 40 keV, with a peak intensity at 27.5 keV. For X-ray imaging, a scintillator–lens–camera configuration was used. A pco.dimax S4 CMOS camera was used for imaging, consisting of a 2016×2016 array of square pixels, each with an $11 \mu\text{m}$ edge length. A long working distance Mitutoyo $2 \times$ lens was used to magnify the

visible light images that were converted from X-ray shadow images by a $100\text{-}\mu\text{m}$ -thick LuAG:Ce scintillator. These factors resulted in isotropic voxels with a $5.5\text{-}\mu\text{m}$ edge length in the tomograms. However, the maximum beam height was 3.4 mm . This resulted in a maximum field of view of approximately $3.4 \times 11 \text{ mm}^2$ at the scintillator, and a cubic $3.4 \times 11 \times 11 \text{ mm}^3$ maximum reconstruction volume. Due to the width of the sample being much less than 11 mm , the recorded images were cropped down in width to only the central 1008 pixels. The tomogram volume, then, was $640 \times 1008 \times 1008$ voxels, or $3.4 \times 5.5 \times 5.5 \text{ mm}^3$. After reconstruction, this volume was cropped down to cover only the sample. The distance from the sample to the scintillator was kept at 15 cm .

Before performing in situ imaging and applying load, a slow scan was performed on the as-printed dogbone samples. For this initial scan, 1,500 evenly spaced images were acquired over a 180° rotation range at a rotation rate of 30° s^{-1} with $900 \mu\text{s}$ exposure for each image. During tensile loading of the sample, the sample and the containing load fixture were rotated continually in a 'tornado scan' fashion, as opposed to a back-and-forth scan motion sometimes referred to as a 'washing machine' scan mode. In order to perform the tornado scan with the loading fixture in place, a slip ring was used for electrical contacts to control and power the fixture's motor and acquire data from the load cell. The rotation rate used for imaging was 500 ms per full rotation, in other words, 720° s^{-1} , or 2 Hz . Once the rotation reached full speed, loading and imaging simultaneously began. During tensile loading, 901 evenly spaced images were acquired over each 180° rotation with a $200\text{-}\mu\text{s}$ exposure and a $255\text{-}\mu\text{s}$ gap between exposures. So, four reconstruction volumes, or tomograms, were acquired for each second of loading, that is, at a rate of 4 Hz . The camera was able to record approximately 45 GB of radiographs before requiring a readout to external memory. The field of view for this experiment was set large enough to comfortably cover the sample cross section, but was minimized for the sake of camera memory, to maximize the number of radiographs/tomograms that could be acquired. In conjunction with the field of view in the radiographs and the number of images acquired per rotation, the camera limited the acquisition to 22 full rotations of imaging, equivalent to 44 tomograms from unique radiographs. At the conclusion of

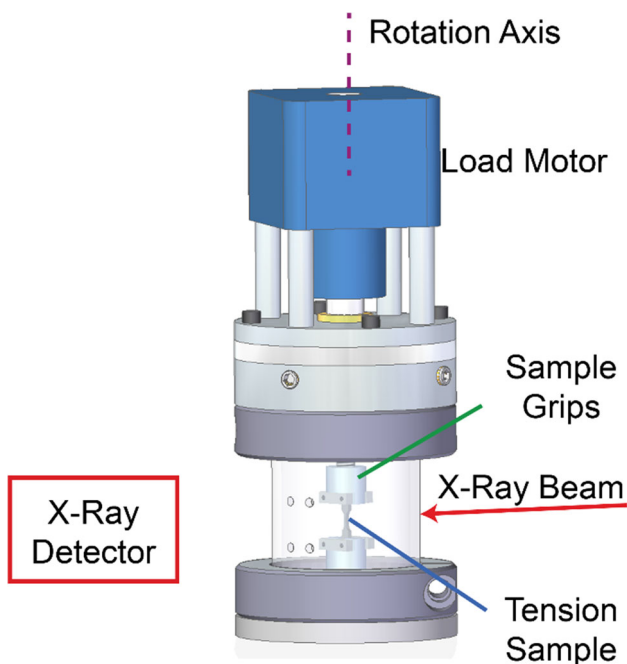


Figure 2 Schematic of beamline and load fixture layout for CT imaging with in situ tensile testing.

imaging, roughly 20 min was required to off load the radiographs, roughly 45 GB, from the camera to a hard disk. During this time, the sample was removed from the loading fixture and a new sample was mounted. In reconstructing the data for analysis, each stack of projections corresponding to each 180° rotation period was input to TomoPy [29] for GRIDREC reconstruction [30], using stripe removal filtering [31] and Paganin phase retrieval [32] in the process.

In situ tensile testing

Dynamic X-ray microtomography imaging was performed on the PA 3200 GF tensile specimens under tension. Due to time constraints, just one sample of each composition and each print direction was tested, yielding nine samples tested in total under dynamic CT. This was made using a custom load fixture shown in Fig. 2. This load fixture has been previously detailed [33] and used for in situ tension studies at a synchrotron imaging beamline [34], where the only difference in this study was the use of slip rings to eliminate any wiring entanglement during the tornado scan rotation. Tensile testing was performed in displacement-control mode, with 3.95 μm steps. A displacement rate of 0.1 mm s^{-1} was used. With the 10 mm gage length of the tensile specimens, this corresponded to a strain rate of 0.01 s^{-1} , or 1% s^{-1} . The manufacturer-specified strain-at-failure for the printed material was 9%, so it was expected that the material would fail after roughly 9 s of imaging, or, after 36 CT datasets with the aforementioned reconstruction method. The load cell count output was calibrated and recorded in Newtons at a rate of 1 kHz. The step size of the motor was 0.006 mm, and maximum force output at 5 V was 500 N.

Digital volume correlation

From in situ CT imaging under mechanical load, a 4D dataset was acquired for each sample. In other words, a 3D tomogram of a region of interest in the gage length existed for each sample at various points throughout its tensile deformation. Given the presence of random, densely distributed, high-contrast, point-like, glass microbead features in the microstructure of the tensile specimens' tomograms, the data enabled application of DVC techniques for

measurement of microscale strain in the region of interest. The Vic-Volume software package (Correlated Solutions) was used to volumetrically map the strain evolution inside the samples during tensile testing. The software used DVC methods, similar to digital image correlation methods for surface-imaging-based method for strain mapping, but with extensions to accommodate for three-dimensional feature tracking and extensions for considering three-dimensional translations and rotations. The details of the DVC method have been described previously [35, 36]. In short, DVC uses a reference state and a deformed state to calculate a three-dimensional displacement field based on automated feature tracking and the voxel size of the image volume. Then, the displacement field is converted to a strain field for the three primary volume directions (ϵ_{xx} , ϵ_{yy} , and ϵ_{zz}) and the three corresponding shear directions (γ_{xy} , γ_{xz} , and γ_{yz}). In this experiment, the loading direction was applied along the gage length, which was parallel to the rotation axis, defined here as being parallel to ϵ_{zz} . In this study, the engineering strain ϵ_{zz} was calculated with a search window of 61 voxels, a subset of 11 voxels, and using the sum of square errors correlation method.

Prior to DVC analysis, but after reconstruction, the in situ datasets for a given sample were cropped to the largest common material volume and aligned manually with respect to a recognizable plane on one side of the failure region. Then, the volumes were filtered in Avizo Fire 9.0.1 (FEI, Visualization Science Group, Burlington, MA) to reduce noise in the images to aid in feature correlation. The reconstructed volumes were filtered with 3D edge-preserving smoothing, followed by 2D non-local means filtering in the reconstruction planes of the tomograms perpendicular to the loading direction, and then subjected to DVC analysis. After correlation between the reference and deformed states for each sample, a strain volume was calculated. The strain volume for each state was masked so as to force 'zero' strain values where in fact no material was present. This was accomplished by creating a mask of the material portion of the tomography volume. The 3D mask was created by segmenting the solid material from the corresponding tomography volume. The mask was then applied to the strain volume. This final step resulted in strain volumes, which had zero values of strain forced on contained porosity, surface porosity, and the air surrounding the sample.

Ex situ tensile testing

In order to test a larger sample population, EOS PA 3200 GF tensile specimens were tested in tension without any imaging, or ex situ. These tests eliminated possible X-ray effects on mechanical properties and allowed a larger sample size to be studied. A CT500 (Deben UK Limited) micromechanical testing fixture was used to measure the miniature tensile specimens' tensile response. Samples of each print orientation were tested for each recycled material composition. The samples were pulled at a rate of 0.1 mm min^{-1} , or $1.67 \text{ } \mu\text{m s}^{-1}$. The load was measured at each displacement step, and the actual displacement of the gage length was inferred from the motor step size and the number of motor steps. Tensile test data and analysis from ex situ testing with a larger sample size than was practical for in situ analysis are presented and discussed in 'Results and analysis' section and 'Discussion' section.

Results and analysis

Microtomography with in situ tensile testing

Mechanical characterization

The reconstructed CT data resulted in 3D images, which captured the key microstructural features in the dogbone samples. In the CT data, the samples' voids, nylon matrix, and glass particles were clearly observed. The voids in the data were the darkest features in the sample, with grayscale values similar to the surrounding air. The polymer matrix was observed as the continuous, intermediate intensity phase across the tomograms. The spherical glass particles appeared as circular features in a given virtual cross-sectional image of the sample volume, and being the most heavily attenuating phase of the tomogram, had the largest intensity of all the

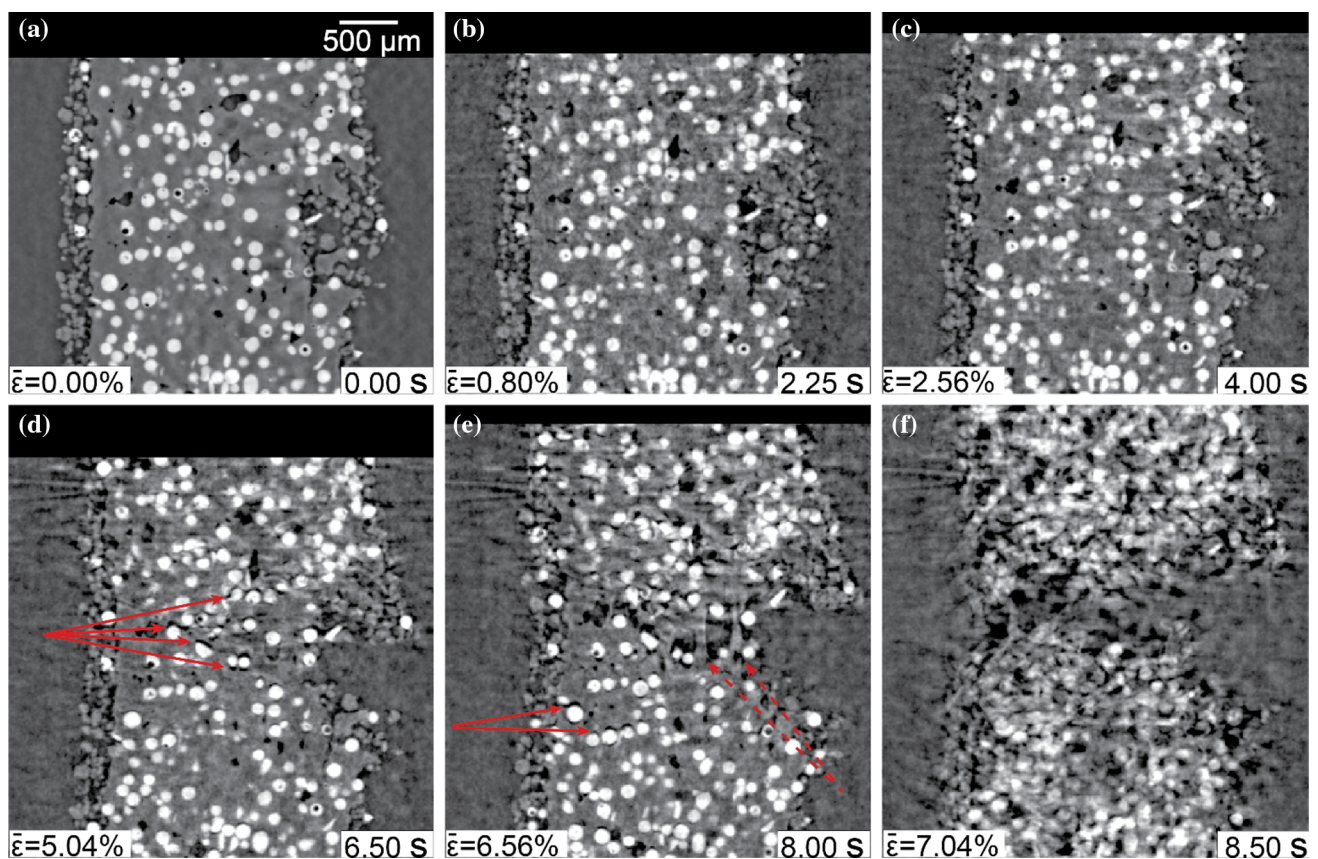


Figure 3 A virtual cross sections through the reconstructed volumes of the X70 sample at various times and average far-field strains throughout the tensile deformation progressing from a undeformed, to f failure, with the *solid red arrows* indicating

particle–matrix separations and the *dashed arrows* emphasizing ligament formations. The *white circles* are the cross sections of the glass particles, the *gray* surrounding is the polyamide. Air is seen on the *right and left*.

features. These features are shown in Fig. 3a for sample X70.

As described in ‘Materials and methods’ section, the sample was imaged in a static condition before beginning dynamic imaging. The static tomogram was derived from a load-free sample, finer angular sampling, and radiographs of longer exposure. As expected, the static CT scans yielded the highest quality tomogram (Fig. 3a). The dynamic tomograms of the samples under tension revealed similar microstructural features, although possessed a greater amount of noise due to the high scan rate and possessed a coarser resolution due to the sample straining during the scans. The blur effect of the in situ tension testing was minimal at the onset of loading, but was exacerbated near total failure of the sample, particularly so for images acquired after the ultimate tensile strength was reached when the strain rate was increased during necking. Near-failure, significant blurring was observed as a result of the samples’ recoil. Figure 3 portrays a fixed cross-sectional region of the dynamic tomograms of sample X70 under tensile loading in the vertical direction at various key stages throughout deformation. This cross section shows the entire width of the sample, and the height of the sample covers roughly 1.7 mm of the sample both above and below the notch, and the cross-sectional image corresponds to the middle position of the sample in the depth direction. The effect of extent of deformation on the image blur is shown in Fig. 3.

The virtual cross sections of X70 shown in Fig. 3 capture the same microstructural features as tensile deformation progresses. The virtual cross sections shown are orthogonal to the axis of the slight notch and taken from the center of the sample. The notch is shown centrally in the images at the right side of the sample. In Fig. 3, loading was in the vertical direction. Figure 3b shows the same cross section as Fig. 3a, but instead of before loading, portrays the sample near the end of its elastic deformation regime after 2.25 s of loading. The deformation captured in Fig. 3b was small and may only be observable in the overall change in the size of the image necessary to capture the same features, which was just a few pixels. Figure 3c shows the same cross section in the early stages of plastic deformation, but before the peak load was reached, after 4.00 s of loading. Here, the deformation occurring is more obvious, but still, no significant damage can be observed in the sample.

When the sample reached its peak load after 6.50 s of tension, the severe deformation and damage of the sample are indisputable, as shown in Fig. 3d. At this stage of tension, the notch at the right was significantly spread, voids appeared to elongate, and particle–matrix separations were observed (solid arrows in Fig. 3). After 8.00 s of loading, as shown in Fig. 3e, the sample approached the end of its plastic deformation. The extent of particle–matrix separation was increased, the matrix was seen to separate, and small ligaments of matrix were seen to branch what became the fracture surfaces (dashed arrows in Fig. 3). Blurring in the tomograms at this stage became significant. Just before ultimate failure after 8.50 s of loading, as shown in Fig. 3f, the tomogram became very heavily blurred due to excess sample motion as the material breaks and elastically recovers, and by this time only a few remaining ligaments were in the process of breaking. A volume rendering of the damage progression is provided in Fig. 4. Throughout tensile deformation, the relative positions of the glass microbeads which were relatively distant from the failure surface are maintained, for example the dense row of three particles indicated by the solid arrow in Fig. 4. Near the failure surface, however, the features become distorted. As indicated by the dashed arrow, a cluster of two microbeads which started out with a strong vertical alignment (Fig. 4a, b) distort into a strong horizontal alignment (Fig. 4c). The ligaments branching the sample halves just before failure are visible in Fig. 4c. As visible in Fig. 4, the particles were never observed to fail; rather, voiding at the interface between the particles and the matrix was observed. These interfacial debonding events were observed around the time the ultimate tensile strength was reached for all print directions and recycled content. As shown in Fig. 4, the failure of tensile specimens was observed to occur by first a slight necking near the notch, followed by interfacial particle debonding in the neck, followed by the formation of branching matrix ligaments between the debonding events, followed by rupture of the matrix ligaments resulting in sample failure. The dynamic CT data for all the samples portrayed similar characteristics as sample X70.

An approximate stress and strain value were sought for each recorded load point. For each sample tested in situ, an average engineering stress was calculated from the load data at each sampling point. Using the static tomogram, the cross-sectional area of

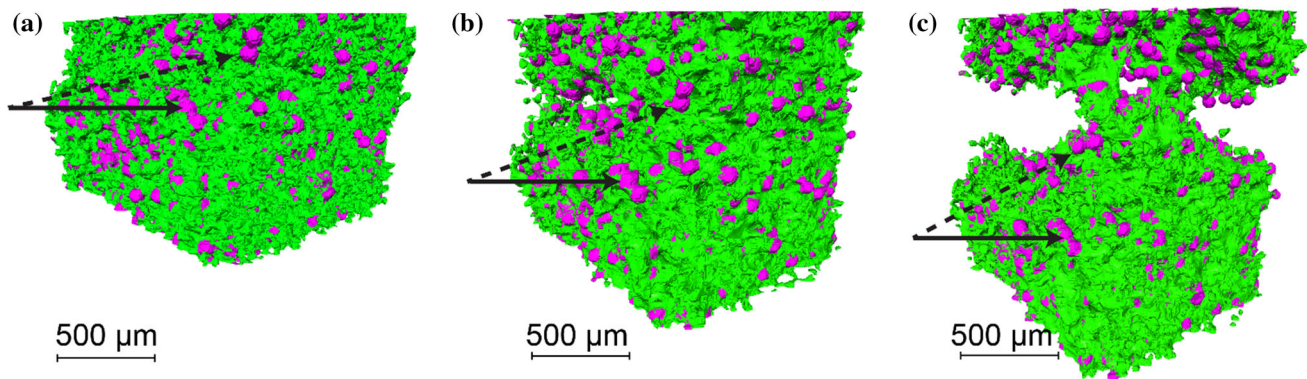


Figure 4 3D renderings based upon the X-ray absorption from dynamic X-ray tomograms of a highly absorbing borosilicate microbead particle (*purple*)-reinforced polyamide-12, moderately X-ray absorbing matrix (*green*) specimen's deformation under

tension, showing **a** the undeformed state, **b** after necking, and **c** immediately preceding failure, with *arrows* provided for particle tracking throughout deformation.

the sample was measured in each slice by segmenting both the glass and nylon phases from the surrounding air and the contained voids. A simple grayscale threshold proved effective with cutoffs between air-polyamide and polyamide-glass of 6087 and 8042 counts, respectively. The average cross-sectional area and area standard deviation were then calculated across the section of the gage length, which was contained in the tomogram. The mean stress was then calculated using the average of the area measurement in the initial, static tomogram. The cross-sectional area statistics of the initial, static tomogram were used for tensile stress calculation at each loading point up to sample failure, that is, an engineering tensile stress calculation was used. In the SLS-derived parts, some residual, unsintered powder material was observed across the surfaces. Visually and qualitatively, this residue appeared relatively minimal and consistent for all of the sample prints. As no repeatable technique was identified for omitting this presumably non-load-bearing material from the cross-sectional measurements, it was incorporated into the measurement of cross-sectional area and engineering stress. This approach was expected to lead to a slight underestimate of engineering stress. Dynamic CT enabled measurement of the displacement at each point using the tomogram itself, by measuring distance changes between features across the tomogram in line with the loading direction. For this study, however, DVC was used to measure local and quasi-far-field (edge of volume) strains in the sample autonomously. Yet, additionally, an approach was taken to approximate the far-field tensile strain,

$\bar{\epsilon}$, in the samples without any imaging knowledge. With this approach, the displacement at each point of loading was approximated using the step size of the loading motor (6 μm) and the number of motor steps applied. Then, the printed gage length was used to approximate the far-field strain, $\bar{\epsilon}$, in the sample at each loading point. This, of course, was an approximation and was expected to be an overestimate of $\bar{\epsilon}$, as some compliance of the loading fixture was expected. Particularly, at the onset of loading, it was observed that motor steps were applied without any increase in the measured load. These initial motor steps were not counted in the displacement approximation. After the load frame was engaged with the motor, it was expected that the system compliance would be most significant at high loads.

Alternatively, the true stress and true strain during dynamic tension testing were also analyzed. Essentially, this method utilized all of the dynamic tomograms. The true strain was calculated by taking the measured load at a given point in tension divided by the minimum cross-sectional area of the sample at the same point in loading. As each tomogram reconstructed corresponded to 0.25 s of loading, an average load in the same time frame was used. The minimum cross-sectional area was calculated using a threshold segmentation of all the solid in the tomogram, over the imaging field of view in the vertical direction. The true stress calculations became controversial after the ultimate tensile strength (UTS) was reached, when the local strain rates were greatest near failure, and the images became heavily blurred. The blurring effect near failure resulted in visible

inaccuracies of the segmentation procedure (see Fig. 3f). For a given sample, the true strain was quantified by tracking two features on either side of the failure region (the notch) in the dynamic tomograms, in the center of the cross sections, throughout loading. The true strain measurement was much more dubious than true stress and was found to vary depending on the range of the gage length used for the measurement. This was a result of the notched region of the gage length dominating the plastic deformation and failure of the sample. Because failure occurred in the notch region, this region was also the focus of measured displacement after plastic onset. Therefore, the further apart the particles used for displacement tracking, the smaller the inferred true strain. For the X100 sample, a comparison between these two methods for stress and strain analysis is provided in Fig. 5. The result shown in Fig. 5 was based on true strain calculation using two features on either side of the notch, equidistant from the notch, with an initial separation of 1.35 mm. In Fig. 5, it can be seen that these two methods produce similar results until plastic onset. One obvious inaccuracy in the true stress versus true strain behavior shown in Fig. 5 is the decrease in true stress near failure, believed to be caused by erroneous, inflated measurement of the cross-sectional area in the tomograms near failure that were plagued with motion artifacts.

For these reasons, the aforementioned methods for approximating the engineering stress and

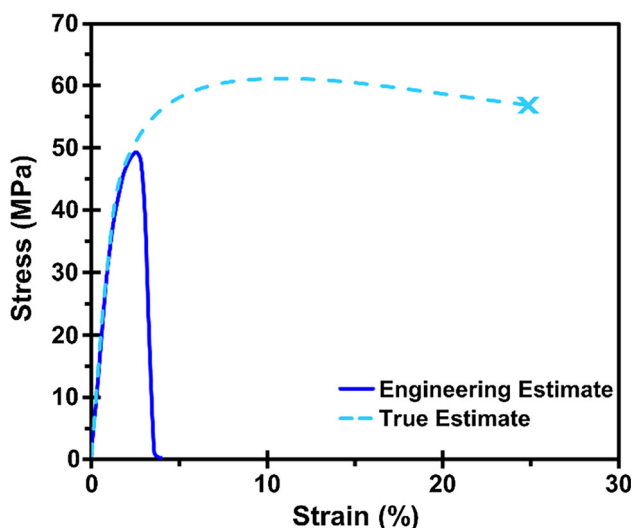


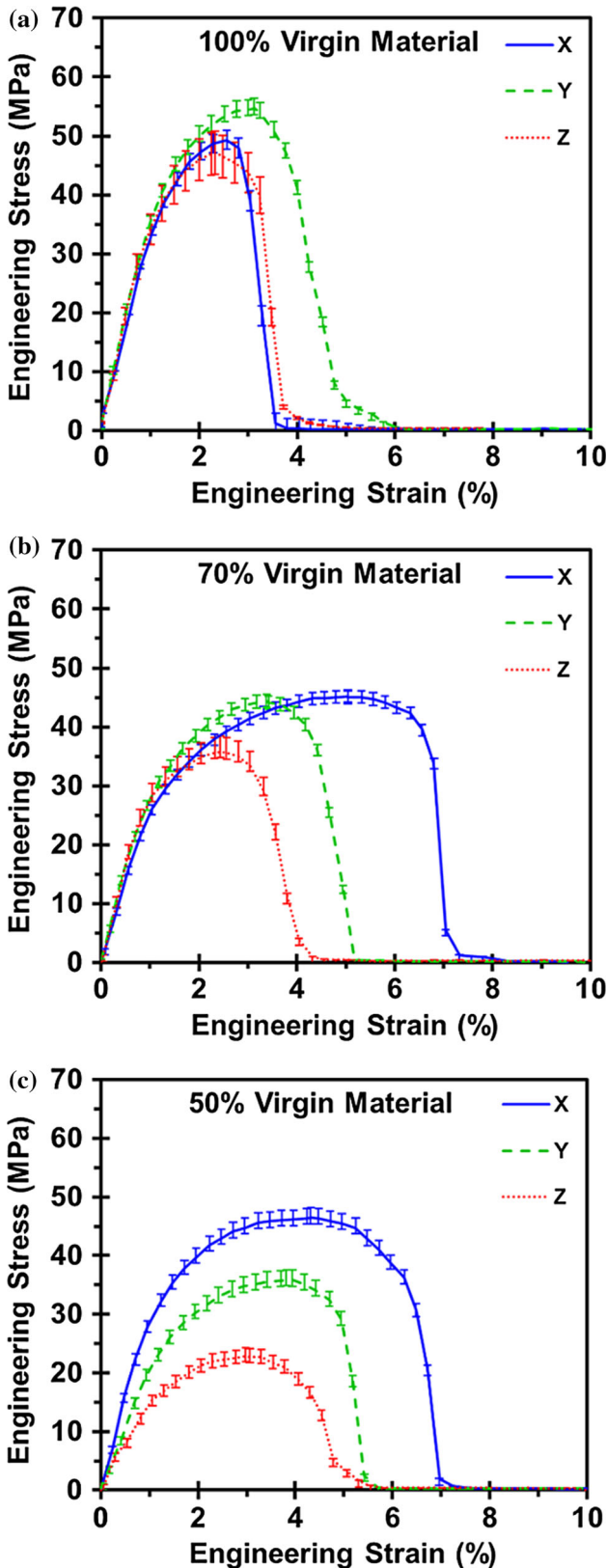
Figure 5 True stress versus true strain and engineering stress versus engineering strain approximations for sample X100.

engineering strain were preferentially implemented for analysis of tensile data acquired under dynamic CT to compare of the different samples' tensile response. Additionally, engineering stress and engineering strain may provide a more direct comparison with other, more traditional results of the PA 3200 GF material, including those which were reported by the manufacturer. The average engineering stress and approximate far-field tensile strain measured by this approach for the in situ tests of all samples are provided in Fig. 6. The stress error bar shown in each direction of the mean stress corresponds to one standard deviation as derived from the cross-sectional variation. To achieve more accurate strain measurements, both locally in the microstructure and in a quasi-far-field fashion, DVC was applied to the dynamic tomograms and is described in 'Digital volume correlation' section. In Fig. 6, the response of the X, Y, and Z anisotropy of the printed tensile specimens is plotted for each virgin/recycled material blend. Figure 6a shows the response of the 100% virgin material, Fig. 6b corresponds to the 70% virgin material blend, and Fig. 6c corresponds to the 50% virgin material blend.

Table 1 summarizes the measured modulus of elasticity, ultimate tensile strength, and strain-to-failure for the samples tested in tension with in situ imaging. The modulus of elasticity was calculated using the slope in the linear regime of the stress versus strain curves. The ultimate tensile strength was simply taken as the maximum mean engineering stress. The strain-to-failure was determined as the approximate far-field engineering strain at which the mean engineering stress dropped below, arbitrarily, 0.5 MPa (Table 2).

Microstructural characterization

With the dynamic CT data, the microstructure of the individual samples was analyzed. Primarily, the character of the porosity and the glass particle reinforcement were probed in attempt to elucidate any otherwise unexpected differences in mechanical behavior. For each sample tested in tension with in situ tomography, the porosity and glass particle reinforcement volume fraction was measured for the portion of the samples, which resided in the imaging field of view. A maximum rectangular sub-volume of the full tomography reconstruction, contained within the sample but not intersecting the surface, was used



◀ **Figure 6** Engineering stress versus engineering strain acquired in situ with microtomography imaging at a strain rate of approximately 0.01 s^{-1} for the X, Y, and Z direction for a 100% virgin material, b 70% virgin material, and c 50% virgin material.

for the analysis, to exclude the air surrounding the sample from the volume measurements. This contained sub-volume was thus nearly 3.4 mm in the height direction, parallel to the imaged samples' gage lengths, and was used for both porosity and particle analysis. The measured values for each sample are provided in Table 3. With the exception of sample Z50, the porosity content varied from 2.9 to 6.2%. Sample Z50 was an extreme outlier, with a porosity of nearly 19%. The porosity is expected to have an effect on the mechanical properties; however, the values reported in Table 1 and Fig. 6 were based on solid cross section only. In other words, the strength, stiffness, and stress values were effectively normalized to take into account the actual amount of material subjected to the tensile load of the tests. For the particle volume fraction values reported in Table 3, the value reported is the percent of glass particle within the solid itself, not taking into account the porosity that was in the material. These values are representative of the powder stock material of the SLS printer on a solids basis. The particle fraction of the solid portions of the tensile specimens ranged between 23.6 and 27.8%, yielding much less sample-to-sample variation than the printed part porosity. Thus, the variations in the samples in terms of particle content were minimal and are not expected to have a significant impact on the mechanical results.

In attempt to quantify the error of the phase analysis, the segmentation was varied to determine the effect on the measured volume fraction of the porosity and the glass particle reinforcement. By dilating each phase three-dimensionally by one voxel from what was a visually optimal segmentation, an upper bound was established. By eroding each phase three-dimensionally by one voxel from what was a visually optimal segmentation, a lower bound was established. This was only performed for one sample, Y100, which was measured to have the median value in terms of porosity. By eroding the pore segmentation, the volume percentage measured for the pore

Table 1 Measured modulus of elasticity (E), ultimate tensile strength (UTS), and strain-to-failure (STF) for PA 3200 GF tensile specimens tested with in situ microtomography at a strain rate of approximately $1 \times 10^{-2} \text{ s}^{-1}$ with a sample size of unity for each measurement

Strain rate (s^{-1})	Virgin content (%)	Print direction	E (GPa)	STF (%)	UTS (MPa)
1×10^{-2}	100	X	3.5	3.8	49.3
1×10^{-2}	100	Y	2.1	6.2	54.6
1×10^{-2}	100	Z	3.9	5.2	47.2
1×10^{-2}	70	X	2.8	8.3	45.2
1×10^{-2}	70	Y	3.2	5.4	44.4
1×10^{-2}	70	Z	3.3	4.8	35.8
1×10^{-2}	50	X	3.2	7.5	46.4
1×10^{-2}	50	Y	2.1	5.7	35.9
1×10^{-2}	50	Z	2.0	5.8	22.9

Table 2 Average measured modulus of elasticity (E), ultimate tensile strength (UTS), and strain-to-failure (STF) for PA 3200 GF tensile specimens tested without imaging ('ex situ')

at a strain rate of approximately $1.7 \times 10^{-4} \text{ s}^{-1}$, showing standard deviation (σ) for some measurements with sample size (n) larger than one

Strain rate (s^{-1})	Virgin content (%)	Print direction	E (GPa)	σ [E] (GPa)	STF (%)	σ [STF] (%)	n [E , STF]	UTS (MPa)	σ [UTS] (MPa)	n [#]
1.7×10^{-4}	100	X	2.0	–	3.1	–	1	35.7	–	1
1.7×10^{-4}	100	Y	2.4	0.0	3.1	0.4	3	36.7	0.9	3
1.7×10^{-4}	100	Z	1.7	0.1	2.6	0.3	2	31.4	1.1	3
1.7×10^{-4}	70	X	2.1	0.0	4.2	0.4	2	30.1	0.5	3
1.7×10^{-4}	70	Y	2.0	0.0	4.1	0.4	3	30.1	0.6	3
1.7×10^{-4}	70	Z	1.8	0.2	3.1	0.0	2	21.1	0.3	3
1.7×10^{-4}	50	X	1.5	0.2	4.6	0.0	2	26.8	2.1	3
1.7×10^{-4}	50	Y	1.5	0.0	5.4	1.1	3	21.5	0.2	3
1.7×10^{-4}	50	Z	1.5	–	5.2	–	1	12.3	0.4	3

Table 3 Phase analysis of porosity and glass particle reinforcement volume fraction for the samples tested in tension with dynamic tomographic imaging, where particle measurement error is estimated $\leq \pm 10\%$ absolute, and the porosity measurement error is estimated $\leq \pm 2.5\%$ absolute

Virgin content (%)	Print direction	Porosity (%)	Particle fraction (%)
100	X	3.3	26.2
100	Y	4.2	24.3
100	Z	4.4	25.8
70	X	2.9	23.6
70	Y	3.1	25.7
70	Z	4.2	25.8
50	X	4.2	27.1
50	Y	6.2	27.8
50	Z	18.7	26.0

phase changed by -2.1% . By dilating the pore segmentation, the volume percentage measured for the pore phase changed by $+2.8\%$. By eroding the particle segmentation, the volume percentage measured for the particle phase changed by -9.1% . By dilating the particle segmentation, the volume percentage measured for the pore phase changed by $+10.6\%$. By visual inspection, the dilation and erosion results for each phase resulted in an extremely inaccurate

segmentation. Nevertheless, the exercise provided some bounds, albeit extremely conservative, for the data reported in Table 3. To summarize, the error of the particle volume percentage measurement was within $\pm 10\%$ absolute, and the error of the porosity measurement was within $\pm 2.5\%$ absolute.

Although the particle volume fraction was not significantly different between samples, the results in Table 3 do not have any implication on whether

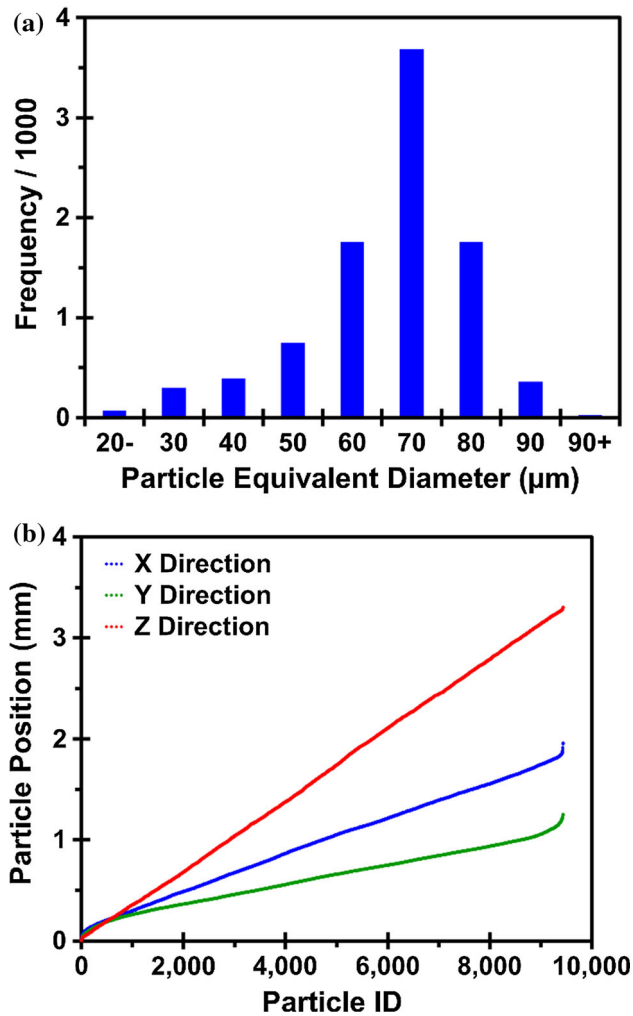


Figure 7 Glass particle analysis for sample X50 showing **a** particle size distribution, and **b** particle locations in three orthogonal directions of the tomography volume.

particle size and extent of clustering were similar between samples. For this analysis, the entire portion of the sample that was within the tomography field of view was utilized, that is, the edges of the sample were not excluded. To determine whether clustering and size varied within the sample population, the particles were subjected to individual analysis. After particle segmentation, the binarized objects were subjected to watershed-based splitting, to differentiate particles which were touching one another. A border-kill operation was then performed to remove features that were obstructed by the volume borders. The equivalent diameter was measured for each individual particle. Figure 7a portrays the distribution of particle size in terms of equivalent diameter for sample X50, which had nearly 10,000 particles in

the volume. Sample X50, as shown in Fig. 7, had a mean equivalent diameter of 61.2 μm , a median of 63.3 μm , with a standard deviation of 13.4 μm . The other samples in the test population did not vary significantly from sample X50. To analyze the distribution of particles and the extent of clustering, the barycenter coordinate of each individual particle was calculated. Then, for every particle, the minimum value for each direction's coordinate list made relative by a zero normalization, and then, each direction's coordinate list was sorted in ascending order. The result of this method is plotted in Fig. 7b for sample X50, showing the x , y , and z coordinate trends for every particle in the tomography volume. For every sample, the trend was predominantly linear without any apparent gaps, indicating that clustering was not significant along any given direction. The x , y , and z image directions in this analysis should not be confused with the X , Y , and Z print directions. The image directions here have the same orientation as the DVC-calculated strain directions provided in 'Digital volume correlation' section. Figure 7b shows that the x and y directions have sigmoid-like tails near at the extreme values of the measured range. This can be explained by the fact that the sample edges in the x and y directions were not defined by the image field of view, whereas the sample edges in the z direction were defined by the field of view in that direction. In other words, this is explained as a surface roughness effect. Apart from at the surface, the dense, linear trend shown for the barycenter coordinate of each particle in each direction suggests that the clustering, if present, was random. The analysis of the other eight samples produced similar linear trends, similarly indicating randomly distributed particles. Particle size and clustering did not appear to be significant factors in any variations of the samples' measured mechanical behavior.

Digital volume correlation

The engineering strain along the loading direction (ϵ_{zz}) was mapped volumetrically for each sample tensile tested with in situ CT imaging using DVC. For each sample, only four tomograms out of the 45 acquired tomograms were utilized. The first of which was the CT from the static scan for each sample, used as the reference volume. The second CT used as input to DVC was the tomogram obtained from the end of the elastic regime. The third CT used as input for

each sample's DVC analysis corresponded to the point in loading approximately half way between plastic onset and ultimate tensile strength in terms of far-field strain. The fourth and final CT analyzed with DVC for each sample corresponded to the point in loading at which the sample reached its ultimate tensile strength. Although analyses of the local strain in the samples at greater extents of deformation were sought, this was unsuccessful. Essentially, the tomograms lacked the temporal resolution to faithfully reconstruct the microstructure and implement feature tracking at points of rapid and drastic deformation. In other words, they were too blurry. Furthermore, the CT volumes near failure were significantly deformed with respect to the undeformed volume and were expected not to correlate well. The small subset of tomograms actually used for DVC was determined sufficient to gain insight into the relationship between the approximated far-field strain and the actual local and quasi-far-field strain present in the samples, and sufficient for visualizing and understanding damage accumulation in the samples.

A comparison of the dynamic tomograms and the calculated ε_{zz} maps is provided in Fig. 8. This comparison shows a virtual cross section through sample Z100 at plastic onset, midway between plastic onset

and maximum stress, and at maximum stress. The orientation of the cross sections is identical to Fig. 3, with the loading parallel to the vertical direction, the cross section orthogonal to the notch axis, and with the cross section corresponding to the middle of the sample. In Fig. 8d, the majority of the sample has ε_{zz} values, which were very close to the approximate far-field engineering strain values, although a small amount of material near the notch exhibits significantly higher ε_{zz} values than the far-field approximations. In Fig. 8e, even more of the sample near the eventual failure site begins to exhibit ε_{zz} values significantly greater than the far-field approximations, even surpassing 10% strain in an appreciable amount of the volume. It can be seen that the regions of strain localization correspond to the regions where failure, or cracking, initiate. Even still, far away from the eventual failure sites, which were far away from the notch, the DVC-calculated ε_{zz} values match closely with the far-field approximations. In Fig. 8f at peak load, very little of the tomogram possesses ε_{zz} values which were near the far-field approximations. The $\varepsilon_{zz} > 10\%$ volume increased and localized around the initiated crack. After crack formation behind the notch, DVC results indicate that the material above and below the formed crack maintain the plastic strain imposed before crack formation, a result that is

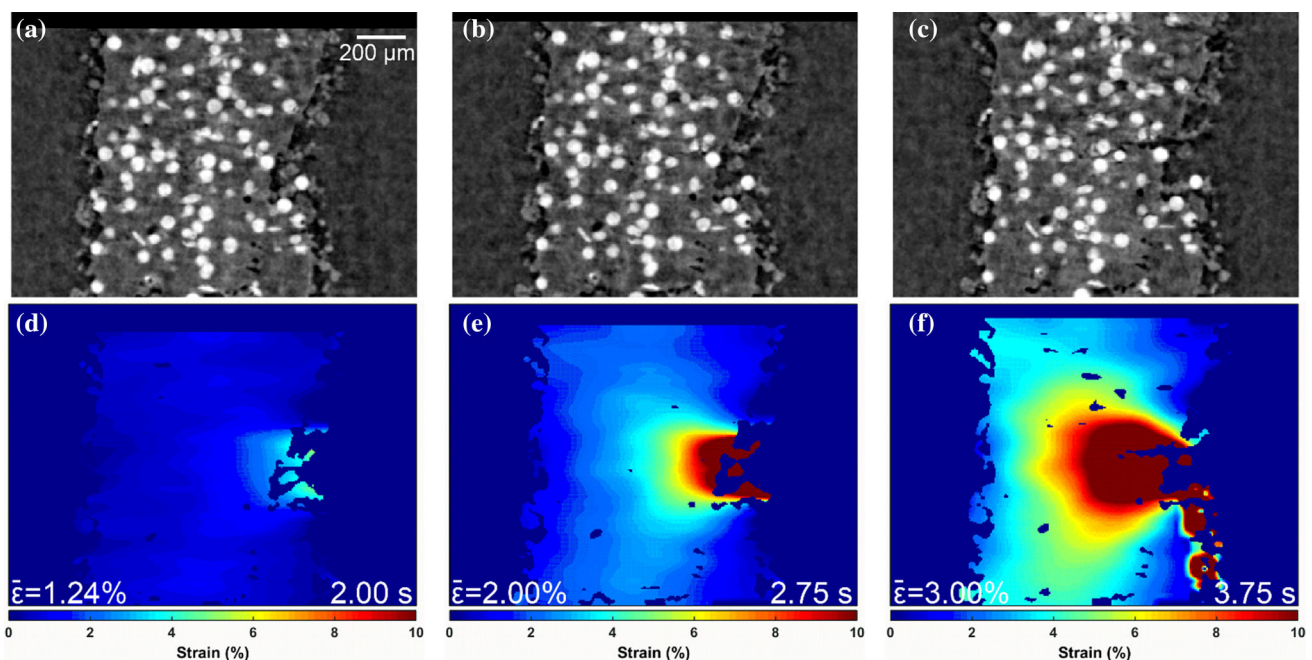


Figure 8 Virtual cross sections of Z100 sample under tension at various times and far-field strain states through the a–c reconstructed sample volumes, and d–f the corresponding DVC-calculated ε_{33} strain-map volumes for the strain parallel to the loading direction.

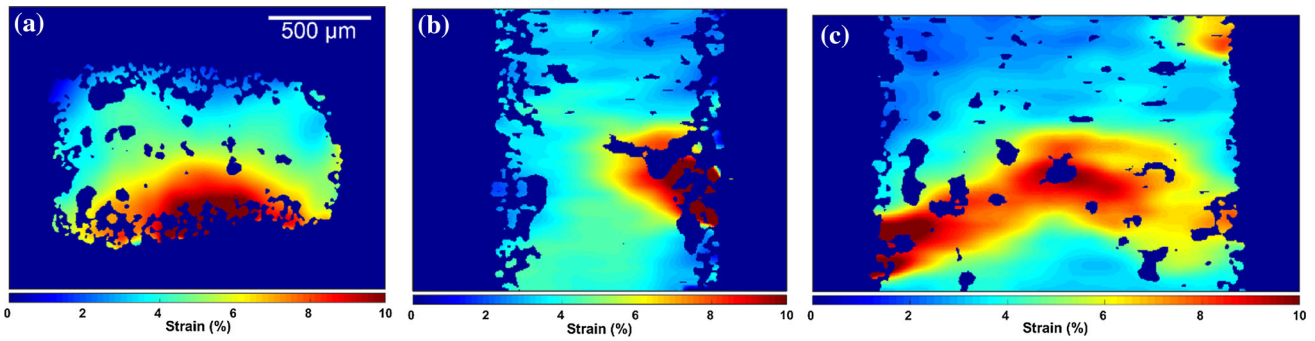


Figure 9 Orthogonal virtual cross sections through the DVC-calculated strain-map volume for the strain parallel to the loading direction (ϵ_{33}) after 2.75 s of tension at a far-field strain of 2.24% for sample X50, located **a** in the notch region and orthogonal to the

loading direction, **b** in the center of the sample and orthogonal to the notch axis, and **c** directly behind the notch and orthogonal to ‘a’ and ‘b’.

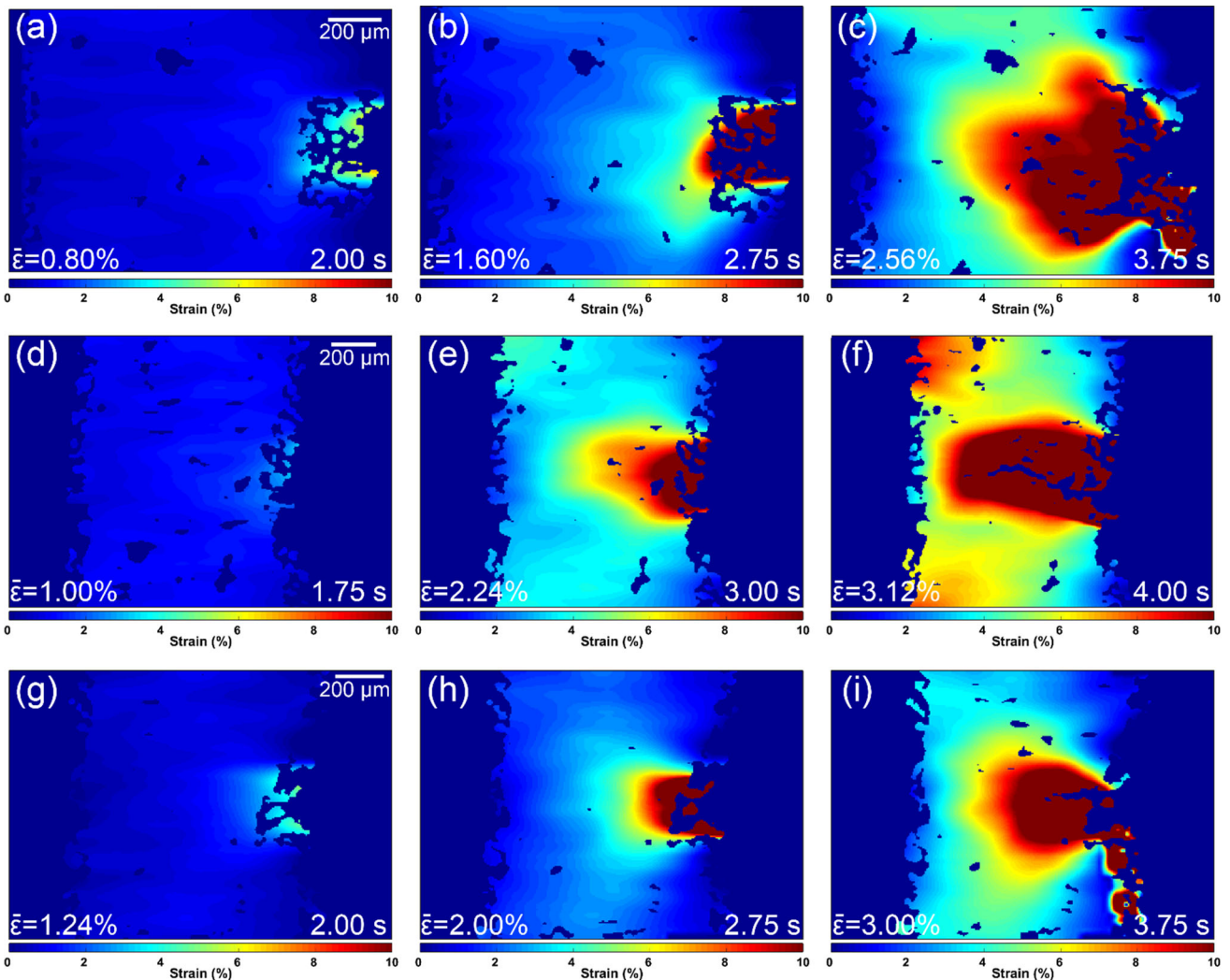


Figure 10 Virtual cross sections through the DVC-calculated strain-map volumes for the strain parallel to the loading direction (ϵ_{33}) for tensile specimens printed 100% virgin material **a–c** in the X direction, **d–f** in the Y direction, and **g–i** in the Z direction,

where the far-field strain state corresponds to **a, d, g** the end of the linear regime, **b, e, h** midway between plastic onset and peak stress, and **c, f, i** at peak stress.

consistent with the unrecoverable nature of plastic deformation. Figure 9 is provided to demonstrate the volumetric nature of the DVC-calculated ε_{zz} maps, which is not well portrayed with a single cross section. Figure 9 shows three orthogonal cross sections of a single ε_{zz} volume generated for sample X50. This figure demonstrates the complex, three-dimensional nature of strain localization near defects in the gage section.

Cross sections of the ε_{zz} volumes are provided for all of the in situ tested samples at plastic onset, midway between plastic onset and peak stress, and at peak stress in Figs. 10, 11 and 12. Figure 10 covers

the directional dependency space for the 100% virgin material, Fig. 11 covers the 70% virgin material samples, and Fig. 12 covers the 50% virgin material samples. DVC is based on feature tracking and is not void of errors or artifacts. Errors in strain mapping from DVC can occur where the algorithm believes to find a feature match from one tomogram to another, but in fact finds a different feature altogether. Some of the artifacts of this technique were found near the sample edges, for example visible below the notch in Fig. 10i, near the bottom of the images in Fig. 11i and Fig. 12c, and near the top of the image in Fig. 11f.

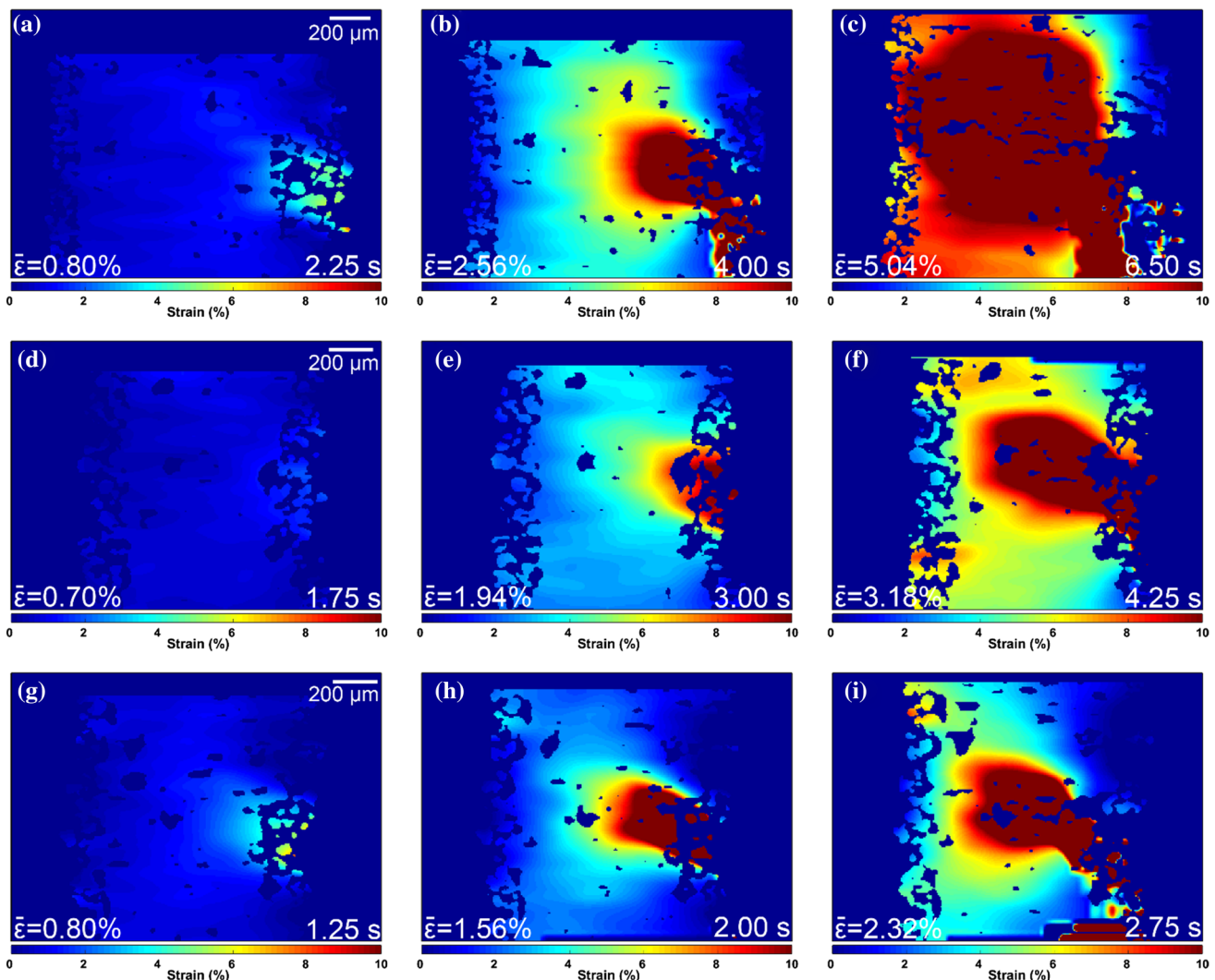


Figure 11 Virtual cross sections through the DVC-calculated strain-map volumes for the strain parallel to the loading direction (ε_{33}) for tensile specimens printed 70% virgin material **a–c** in the X direction, **d–f** in the Y direction, and **g–i** in the Z direction,

where the far-field strain state corresponds to **a, d, g** the end of the linear regime, **b, e, h** midway between plastic onset and peak stress, and **c, f, i** at peak stress.

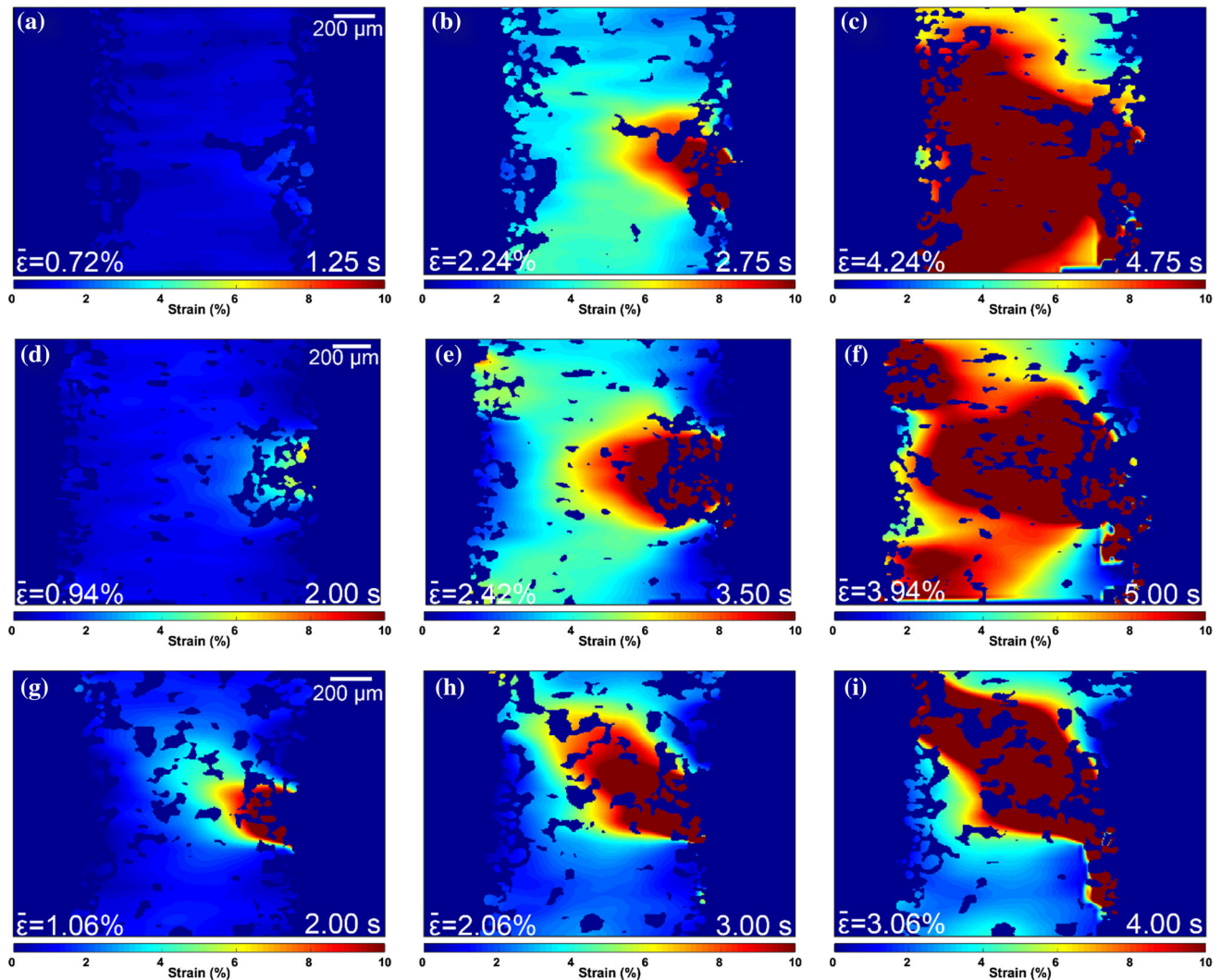


Figure 12 Virtual cross sections through the DVC-calculated strain-map volumes for the strain parallel to the loading direction (ϵ_{33}) for tensile specimens printed 50% virgin material **a–c** in the X direction, **d–f** in the Y direction, and **g–i** in the Z direction,

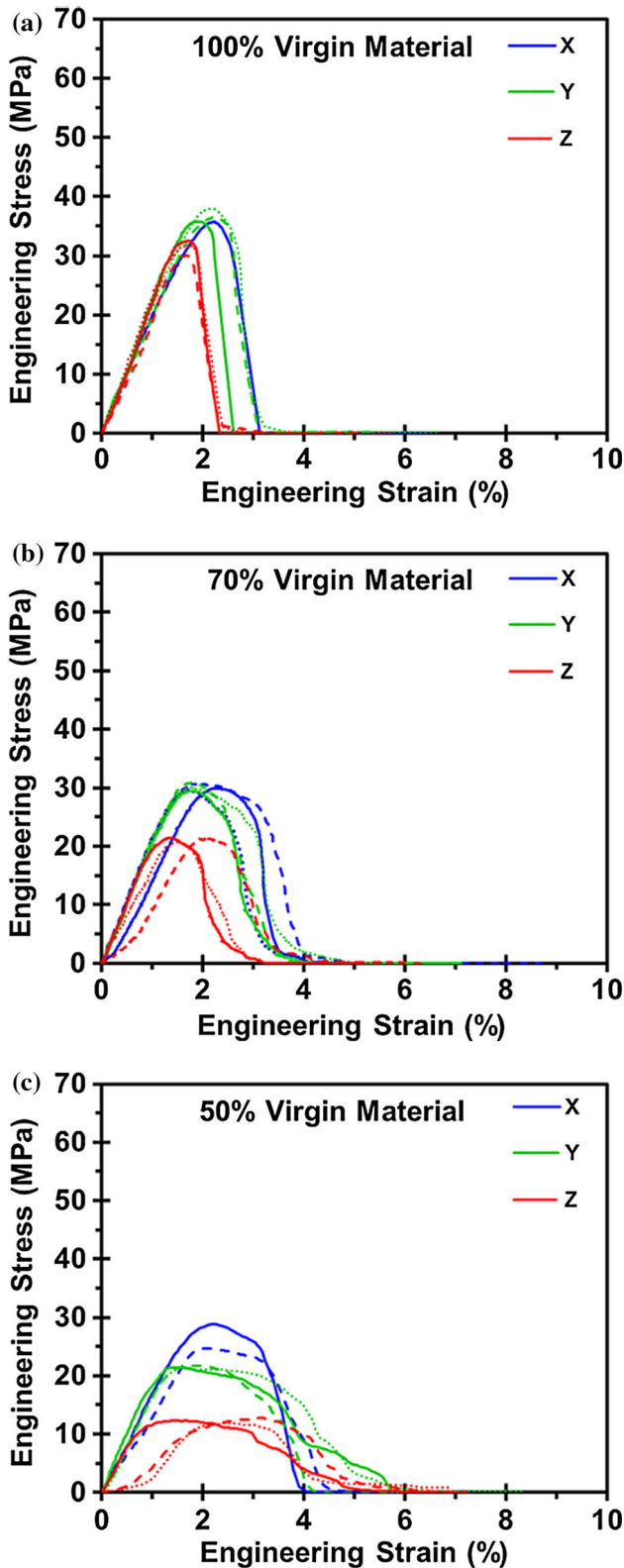
where the far-field strain state corresponds to **a, d, g** the end of the linear regime, **b, e, h** midway between plastic onset and peak stress, and **c, f, i** at peak stress.

Ex situ tensile testing

Due to experimental constraints at the synchrotron beamline and the challenges of big-data analysis, the number of samples per print variable tested with in situ CT was limited to one. A larger sample size was used for tensile testing without imaging. Engineering stress values were approximated from load values in the ex situ tests by using the average cross-sectional area measurements of the CT data of the same sample types. Similar to the in situ approach, the engineering strain values were approximated using the tension motor’s displacement and the gage length of the tensile specimens. Shown in Fig. 13 are

the results of the ex situ tension testing. In Fig. 13, the response of the X, Y, and Z anisotropy of the printed tensile specimens is plotted for each virgin/recycled material blend. Figure 13a shows the response of the 100% virgin material, Fig. 13b corresponds to the 70% virgin material blend, and Fig. 13c corresponds to the 50% virgin material blend. No error bars are shown in this plot to aid in visualization of the variations in repeat tests.

Table 2 summarizes the approximate modulus of elasticity, ultimate tensile strength, and strain-to-failure for the samples tested in tension with ex situ imaging. The modulus of elasticity was calculated using the slope in the linear regime of the stress



◀ **Figure 13** Engineering stress versus engineering strain acquired ex situ at a strain rate of approximately $1.7\text{E}-4\text{ s}^{-1}$ for the X, Y, and Z direction for **a** 100% virgin material, **b** 70% virgin material, and **c** 50% virgin material, showing repeat tests with *dots and dashes*.

versus strain curves. The ultimate tensile strength was simply taken as the maximum engineering stress. The strain-to-failure was determined as the approximate far-field engineering strain at which the mean engineering stress dropped below, arbitrarily, 0.5 MPa. Samples that appeared to have an anomalous, delayed deformation onset were excluded from the modulus of elasticity and strain-to-failure average values reported in Table 2. The number of samples taken in the averaging measurements, n , and the measurement standard deviation, σ , for the ex situ tests are provided in Table 2.

Discussion

In situ tensile testing

For the 100% virgin material samples, the mechanical behavior is fairly isotropic, though sample Y100 appears to exhibit slightly higher strength and ductility than X100 and Z100. Relative to the 100% virgin material samples, the 70% virgin material samples exhibit a measurable decrease in UTS for all print directions. Although sample X70 exhibited a much higher strain-to-failure than sample X100, no significant difference in strain-to-failure is observed between samples Y70 and Y100 or samples Z70 and Z100. In the 70% virgin material sample class, the Z direction appears to be most negatively affected by the addition of recycled material with respect to UTS. In the 50% virgin material class, sample X50 shows negligible difference to sample X70 in terms of UTS and strain-to-failure. With respect to sample Y70, sample Y50 had a measurably lower UTS, but no significant change in strain-to-failure. With respect to sample Z70, sample Z50 showed a significant decrease in UTS and an increase in strain-to-failure.

Across the sample population, the most significant effect of recycled content is manifested in Z direction samples. The addition of recycled material appears to

reduce the UTS of the Z direction from comparable to the X and Y directions to that of significantly lower. Conceivably, the Z direction properties may be fundamentally different than the X and Y directions, because the SLS technique renders this orientation unique in that it is the slowest (between-layer) sintering direction. It can be seen that the Y direction's UTS relative to that of the X direction's appears to evolve from somewhat higher to somewhat lower with increasing recycled material content. Finally, the X direction, being the fast sintering direction, appears to be least affected by the recycled content in terms of strength. The higher UTS of Y100 with respect to X100 is suspected to be potentially based on variations in the samples, as this is not explainable with the rest of the observed trends in sample strength. This observation must be confirmed with a larger sample population.

Digital volume correlation

The application of DVC to the dynamic CT data confirms that strain localizes around the defects present in the gage section of the tensile specimens. Although an intentionally placed notch is ideal for capturing failure events with limited field-of-view imaging, it did result in reduced mechanical performance. The far-field strain $\bar{\epsilon}$ in the gage length at failure is seen to be substantially lower than the local strain ϵ_{zz} which is measured throughout tensile testing. In other words, while the samples failed at $\bar{\epsilon}$ of 3–8%, strains of greater than 10% were measured locally near the failure site. The DVC strain maps also demonstrated the capability to predict wherein the material the failure eventually occurred. While DVC data are strictly quantitative, the present report makes only qualitative observations of these results, and the perceived errors in mapping near the edge of the sample, while inconsequential to the conclusions of this report, should be noted as a possible limitation in quantitative analysis of three-dimensional strains mapped in the present work. However, in the DVC maps, as the distance away from the failure site increases, the local ϵ_{zz} value appears to converge with the $\bar{\epsilon}$ value. The results of DVC demonstrate that strain localization is complex throughout the sample, seemingly clustered around void defects within the material.

In the material printed with 50% virgin materials, the highest recycled content explored, the bands of

strain localization spanned relatively large distances away from the initiation of strain localization, branching relatively far above and far below the notch region in the dogbone samples. This phenomena is shown, for example, in Fig. 12c, f, i. In one interesting case, the bands were manifested in distinct, separated, and somewhat symmetric regions, visible in Fig. 12g. This large vertical spanning was not apparent for the material printed with less recycled powder bed content, perhaps with the exception of sample X70 (Fig. 11d).

The DVC volumes were masked using a segmented volume of the solid phases from the sample tomograms, so that the resulting strain maps only corresponded to points that had yet to fail. Additionally, DVC results were only presented here up to the ultimate tensile strength, when the sample deformation was relatively small. Only the DVC results up to the ultimate strength were believed to be credulous, as significant amount of motion artifacts were present in the proceeding dynamic tomograms. From the results provided in Figs. 10, 11 and 12, the challenge of manually and accurately measuring true strain is apparent; that is, the effect of the reference length used on the measured value can be inferred in the variation of ϵ_{zz} across the sample.

Ex situ tensile testing

In the ex situ testing, it was possible to test multiple samples of identical recycled content and print orientation. In general, the behavior seemed very repeatable, that is, there was not a significant variation in the mechanical behavior for repeat tests (Fig. 13). For the 100% virgin material samples, the mechanical behavior is fairly isotropic, though the Z100 samples appear just slightly weaker. With increasing recycled material content, the UTS of the X samples was least reduced, the UTS of the Y samples was somewhat reduced, and the UTS of the Z samples was drastically reduced. As mentioned in 'In situ tensile testing' section, this appears to be related to the sintering speed in the build of the part, where X is the fastest print direction and Z is the slowest. Whereas the strain-to-failure of the X direction samples seemed to drastically increase with recycled content in the in situ tests, this effect was much more moderate in the ex situ measurements of a larger sample population. The ex situ tests also suggest that the higher strength observed for in situ

sample Y100 relative to in situ sample X100 was anomalous.

Relative to the in situ tests, the ex situ tensile tests were conducted at a 60 times slower strain based on differences in testing equipment. The strain rate dependence appears significant, where the tests conducted at the higher strain rate appear to have roughly 50% greater UTS and strain-to-failure values. From the literature, a reduction in yield strength at lower strain rates has been observed for polyamide-6 [37] and particle composites of polyamide-6 [38], and this is expected to similarly translate to the UTS of polyamide-12. Yet, lower strain-to-failure values at slower strain rates are not expected [39]. At slower strain rates, strain-to-failure is expected to be the same if failure is dominated by the notch, or larger if enhanced by matrix recovery. Possibly, the higher apparent strain to failures in the in situ data is a result of higher instrument compliance, although this is unclear. Alternatively, it could be that the lower strain to failures in the ex situ data was due to sample misalignment or other experimental errors, but this seems unlikely to have been the case with such consistent difference between the two different testing methods. The prior appears to be a more likely artifact because the far-field strain values were mere approximations based on motor displacement, as discussed in ‘[Microtomography with in situ tensile testing](#)’ section. However, within both ex situ and in situ analysis, respectively, the main parameters of the current study (the combined effects of recycled content and print direction) appear to have trends, which hold true between both testing methods.

Conclusions

The tensile properties of an additively manufactured particle-reinforced polymer matrix composite material was studied using in situ synchrotron X-ray computed microtomography, achieving a high temporal resolution of 4 Hz. The effects of recycled source material with a thermal history in SLS were investigated for the three primary sintering, or printing, directions. High-speed CT imaging enabled a qualitative analysis of the deformation and damage processes, including initiation and propagation of interfacial voiding between the matrix and particle phases, matrix pore elongation, and matrix cracking in the composite material. Failure occurred in all the

tensile specimens through the following sequence: slight necking in the area of minimal as-printed cross section, matrix–particle debonding in the neck, formation of matrix ligaments that branched the neck between the debonding sites, and ultimate failure of the sample after failure of the ligaments.

The mechanical data recorded during the dynamic CT imaging provided insight into the effects of recycled material and sintering direction. It was found that tensile properties in the layer-to-layer direction of the SLS parts were comparable to the in-layer directions for parts printed without using any recycled material. However, it was found that the between-layer strength of the printed composites was degraded significantly with respect to the in-layer directions with the addition of recycled material and that the addition of recycled material had at least a slight degradation effect on the strength of the printed composite along all print directions. Within the print plane, in the X and Y directions, the slower of the sintering directions (Y direction) was found to be more affected by the incorporation of recycled material in terms of strength. For this material, the tension results suggest that the effect of recycled material from the SLS print bed degrades the strength in all print directions, but with increasing severity for the slower print direction.

Tensile testing was also performed ex situ, and the results of these tests provided insight into the repeatability of the tensile properties for the SLS composite material. The ex situ tests also provided an understanding of the strain rate dependence in these materials, showing that a viscoplastic behavior existed and that higher strain rates provided higher ultimate tensile strength. The difference in strength at the two different strain rates applied appears in line with the literature reports for nylon. The strain-to-failure difference, however, was found to be contrary to expected strain rate effects. The effect of strain rate on absolute strength and absolute strain-to-failure in the present study was convoluted by possible effects of X-ray degradation. Most importantly, the ex situ tensile testing verified the anisotropy and recycled content trends observed with a limited number of in situ tests of the additively manufactured glass particle-reinforced nylon matrix composites.

The application of DVC enabled quantitative analysis of the deformation and damage present in the samples imaged with microtomography with in situ tensile testing. The DVC results demonstrated

that the calculated ε_{zz} strain volumes were able to map out local strain values, quantify strain localization, and even predict where failure would occur in the material. The locally measured strain values appear reasonable with respect to the far-field strain approximations. DVC analysis of the in situ microtomography images revealed qualitatively that in the material with high recycled powder bed content, bands of high tensile strain formed more in line with the loading direction, traversing the SLS print planes.

The manufacturer specified a strain-to-failure of 9% using the engineering definition, which is greater than the result of the engineering strain analysis method for either the in situ or ex situ measurements in this work. This is conceivably due to the presence of flaws including the intentional surface notch. Unintentional print porosity was also observed in the samples, another flaw which is likely to significantly influence the measured strain-to-failure. Future work should focus on repeating this experiment on material with even less print porosity, with varying strain rate both with and without X-ray exposure, incorporating all the DVC shear and normal strain results in the analysis, and with repeat tests of identical samples under identical test conditions.

Acknowledgements

Los Alamos National Laboratory is operated by Los Alamos National Security LLC under Contract Number DE-AC52-06NA25396 for the US Department of Energy. This research used resources of the Advanced Photon Source, a US Department of Energy (DOE) Office of science User Facility operated for the DOE Office of Science by Argonne National Laboratory under Contract No. DE-AC02-06CH11357, Proposal Number 46200. Funding for this research was provided by the Enhanced Surveillance Campaign, Tom Zocco, Program Manager and the Engineering Campaign, Antranik Siranosian, Program Manager.

Compliance with ethical standards

Conflicts of interest The authors declare no conflicts of interest or bias for the submitted work.

References

- [1] Gibson I, Rosen DW, Stucker B (2010) Additive manufacturing technologies. Springer, New York, pp 1–3
- [2] Zhai Y, Lados DA, LaGoy JL (2014) Additive manufacturing: making imagination the major limitation. *JOM* 66(5):808–816
- [3] SpaceX launches 3D-printed part to space, creates printed engine chamber. (2016) SpaceX. N.p., Web. 2 2016
- [4] Atzeni E, Salmi A (2012) Economics of additive manufacturing for end-usable metal parts. *Int J Adv Manuf Technol* 62(9–12):1147–1155
- [5] Heidi P, Thomas W, Ari H, Jari J, Antti S, Petri K, Olli N (2013) Digital design process and additive manufacturing of a configurable product. *Adv Sci Lett* 19(3):926–931
- [6] Smith H (2013) 3D printing news and trends: GE aviation to grow better fuel nozzles using 3D printing. *3dprintingreviews.blogspot.co.uk*. N.p. Web. 2 June 2016
- [7] Horn TJ, Harrysson OL (2012) Overview of current additive manufacturing technologies and selected applications. *Sci Prog* 95(3):255–282
- [8] Hague R, Campbell I, Dickens P (2003) Implications on design of rapid manufacturing. *Proc Inst Mech Eng C J Mech Eng Sci* 217(1):25–30
- [9] Doubrovski Z, Verlinden JC, Geraedts JM (2011) Optimal design for additive manufacturing: opportunities and challenges. In: ASME 2011 international design engineering technical conferences and computers and information in engineering conference. American Society of Mechanical Engineers, pp 635–646
- [10] Kruth JP, Leu MC, Nakagawa T (1998) Progress in additive manufacturing and rapid prototyping. *CIRP Ann Manuf Technol* 47(2):525–540
- [11] Lü L, Fuh JYH, Wong YS (2001) Selective laser sintering. Springer, New York, pp 89–142
- [12] Bremen S, Meiners W, Diatlov A (2012) Selective laser melting. *Laser Tech J* 9(2):33–38
- [13] Thrimurthulu K, Pandey PM, Reddy NV (2004) Optimum part deposition orientation in fused deposition modeling. *Int J Mach Tools Manuf* 44(6):585–594
- [14] Frazier WE (2014) Metal additive manufacturing: a review. *J Mater Eng Perform* 23(6):1917–1928
- [15] Dotchev K, Yusoff W (2009) Recycling of polyamide 12 based powders in the laser sintering process. *Rapid Prototyp J* 15(3):192–203
- [16] Carroll BE, Palmer TA, Beese AM (2015) Anisotropic tensile behavior of Ti–6Al–4V components fabricated with directed energy deposition additive manufacturing. *Acta Mater* 87:309–320

- [17] Holesinger TG, Carpenter JS, Lienert TJ, Patterson BM, Papin PA, Swenson H, Cordes NL (2016) Characterization of an aluminum alloy hemispherical shell fabricated via direct metal laser melting. *JOM* 68:1–12
- [18] Ahn SH, Montero M, Odell D, Roundy S, Wright PK (2002) Anisotropic material properties of fused deposition modeling ABS. *Rapid Prototyp J* 8(4):248–257
- [19] Adamczak S, Bochnia J, Kaczmarska B (2015) An analysis of tensile test results to assess the innovation risk for an additive manufacturing technology. *Metrol Meas Syst* 22(1):127–138
- [20] Guessasma S, Belhabib S, Nouri H (2015) Significance of pore percolation to drive anisotropic effects of 3D printed polymers revealed with X-ray μ -tomography and finite element computation. *Polymer* 81:29–36
- [21] Khademzadeh S, Carmignato S, Parvin N, Zanini F, Bariani PF (2016) Micro porosity analysis in additive manufactured NiTi parts using micro computed tomography and electron microscopy. *Mater Des* 90:745–752
- [22] Smith DH, Bicknell J, Jorgensen L, Patterson BM, Cordes NL, Tsukrov I, Knezevic M (2016) Microstructure and mechanical behavior of direct metal laser sintered Inconel alloy 718. *Mater Charact* 113:1–9
- [23] Sercombe TB, Xu X, Challis VJ, Green R, Yue S, Zhang Z, Lee PD (2015) Failure modes in high strength and stiffness to weight scaffolds produced by selective laser melting. *Mater Des* 67:501–508
- [24] Leuders S et al (2013) On the mechanical behaviour of titanium alloy TiAl6V4 manufactured by selective laser melting: fatigue resistance and crack growth performance. *Int J Fatigue* 48:300–307
- [25] Sterling AJ, Torries B, Seely DW, Lugo M, Shamsaei N, Thompson SM (2015) Fatigue behavior of Ti–6Al–4V alloy additively manufactured by laser engineered net shaping. In: Proceedings of the 56th AIAA/ASCE/AHS/ASC structures, structural dynamics, and materials conference, Kissimmee, FL
- [26] Patterson BM, Cordes NL, Henderson K, Williams JJ, Stannard T, Singh SS, Ovejero AR, Xiao X, Robinson M, Chawla N (2016) In situ X-ray synchrotron tomographic imaging during the compression of hyper-elastic polymeric materials. *J Mater Sci* 51(1):171–187. doi:10.1007/s10853-015-9355-8
- [27] Patterson BM, Henderson K, Gilbertson RD, Tornga S, Cordes NL, Chavez ME, Smith Z (2014) Morphological and performance measures of polyurethane foams using X-ray CT and mechanical testing. *Microsc Microanal* 20(04):1284–1293
- [28] Karlsson J, Sjögren T, Snis A, Engqvist H, Lausmaa J (2014) Digital image correlation analysis of local strain fields on Ti6Al4V manufactured by electron beam melting. *Mater Sci Eng A* 618:456–461
- [29] Gürsoy D, De Carlo F, Xiao X, Jacobsen C (2014) TomoPy: a framework for the analysis of synchrotron tomographic data. *J Synchrotron Radiat* 21(5):1188–1193
- [30] Dowd BA, Campbell GH, Marr RB, Nagarkar VV, Tipnis SV, Axe L, Siddons DP (1999) Developments in synchrotron X-ray computed microtomography at the national synchrotron light source. In: SPIE's International symposium on optical science, engineering, and instrumentation. International Society for Optics and Photonics, pp 224–236
- [31] Münch B, Trtik P, Marone F, Stampanoni M (2009) Stripe and ring artifact removal with combined wavelet–Fourier filtering. *Opt Express* 17(10):8567–8591
- [32] Paganin D, Mayo SC, Gureyev TE, Miller PR, Wilkins SW (2002) Simultaneous phase and amplitude extraction from a single defocused image of a homogeneous object. *J Microsc* 206(1):33–40
- [33] Singh SS, Williams JJ, Hruba P, Xiao X, De Carlo F, Chawla N (2014) In situ experimental techniques to study the mechanical behavior of materials using X-ray synchrotron tomography. *Integr Mater Manuf Innov* 3(1):1–14
- [34] Williams JJ, Chapman NC, Jakkali V, Tanna VA, Chawla N, Xiao X, De Carlo F (2011) Characterization of damage evolution in SiC particle reinforced Al alloy matrix composites by in situ X-ray synchrotron tomography. *Metall Mater Trans A* 42(10):2999–3005
- [35] Bay BK, Smith TS, Fyhrie DP, Saad M (1999) Digital volume correlation: three-dimensional strain mapping using X-ray tomography. *Exp Mech* 39(3):217–226
- [36] Bay BK (2008) Methods and applications of digital volume correlation. *J Strain Anal Eng Des* 43(8):745–760
- [37] Shan GF, Yang W, Yang MB, Xie BH, Feng JM, Fu Q (2007) Effect of temperature and strain rate on the tensile deformation of polyamide 6. *Polymer* 48(10):2958–2968
- [38] Sumita M, Shizuma T, Miyasaka K, Ishikawa K (1983) Effect of reducible properties of temperature, rate of strain, and filler content on the tensile yield stress of nylon 6 composites filled with ultrafine particles. *J Macromol Sci B Phys* 22(4):601–618
- [39] Li Z, Lambros J (2001) Strain rate effects on the thermo-mechanical behavior of polymers. *Int J Solids Struct* 38(20):3549–3562